Supplementary Information for:

Unveiling the Nature of Room-Temperature-Fabricated p-Type SnO Thin Films: The Critical Role of Intermediate Phases, Lattice Disorder, and Oxygen Interstitials

Mochamad Januar,[†] Cheng-Yu Lu,[‡] Horng-Chih Lin,[¶] Tsung-Yu Huang,*,[‡]

Chia-Ming Yang,*,[†,‡,§,∥,⊥,#] Kuo-Kang Liu,[@] and Kou-Chen Liu*,[†,△,‡,∇]

E-mail: huang.tsungyu@mail.mcut.edu.tw; cmyang@mail.cgu.edu.tw; jacobliu@mail.cgu.edu.tw

Phone: +886-3-211-8800 (ext. 3152). Fax: +886-3-211-8507

S1 Tauc and Urbach Methods

The optical bandgaps, encompassing both direct and indirect types, were determined using the Tauc method based on the following equation (see Figure S1 for detailed fittings):[1]

$$(\alpha \cdot h\nu)^{1/\gamma} = B\left(h\nu - E_{\text{gap}}\right) \ . \tag{S1}$$

Here, h is the Planck constant, ν is the photon's frequency, E_{gap} the bandgap energy, and B is a constant. The γ depends on the nature of the electron transition, being 1/2 for direct and 2 for indirect transition bandgaps. Additionally, the absorption coefficient spectra of the SnO film, with thickness d, were determined using the Beer-Lambert relation: $\alpha = -\frac{1}{d}\ln(T)$, where T is the transmittance.

Additionally, utilizing the same α, information about defects in the film, reflected in the Urbach energy (E_{U}), is obtained from the exponential relationship as follows:

$$\alpha(h\nu) = \alpha_0 \exp\left(\frac{h\nu - E_{\text{gap}}}{E_{\text{U}}}\right) \ , \tag{S2}$$

where α_0 is a constant.

S1.1 Determining the Fitting Range for Urbach Energy Calculation

Previous researches[2–5] have demonstrated that the efficacy of exponential function fitting is constrained by the selection of a limited fitting range. To guide the selection of the fitting range, one can employ the Tauc model,[6] which delineates three distinct energy regions in a semilogarithmic plot of optical absorption, as illustrated in Figure S2. The lowest energy region, labeled 'A', is characterized by an absorption coefficient linked to the excitation of localized electrons from deep levels to the conduction band. In contrast, the high energy region 'C' pertains to the transition of bound valence electrons into a free carrier state in the conduction band. The intermediate region 'B' encompasses the indirect bandgap as well
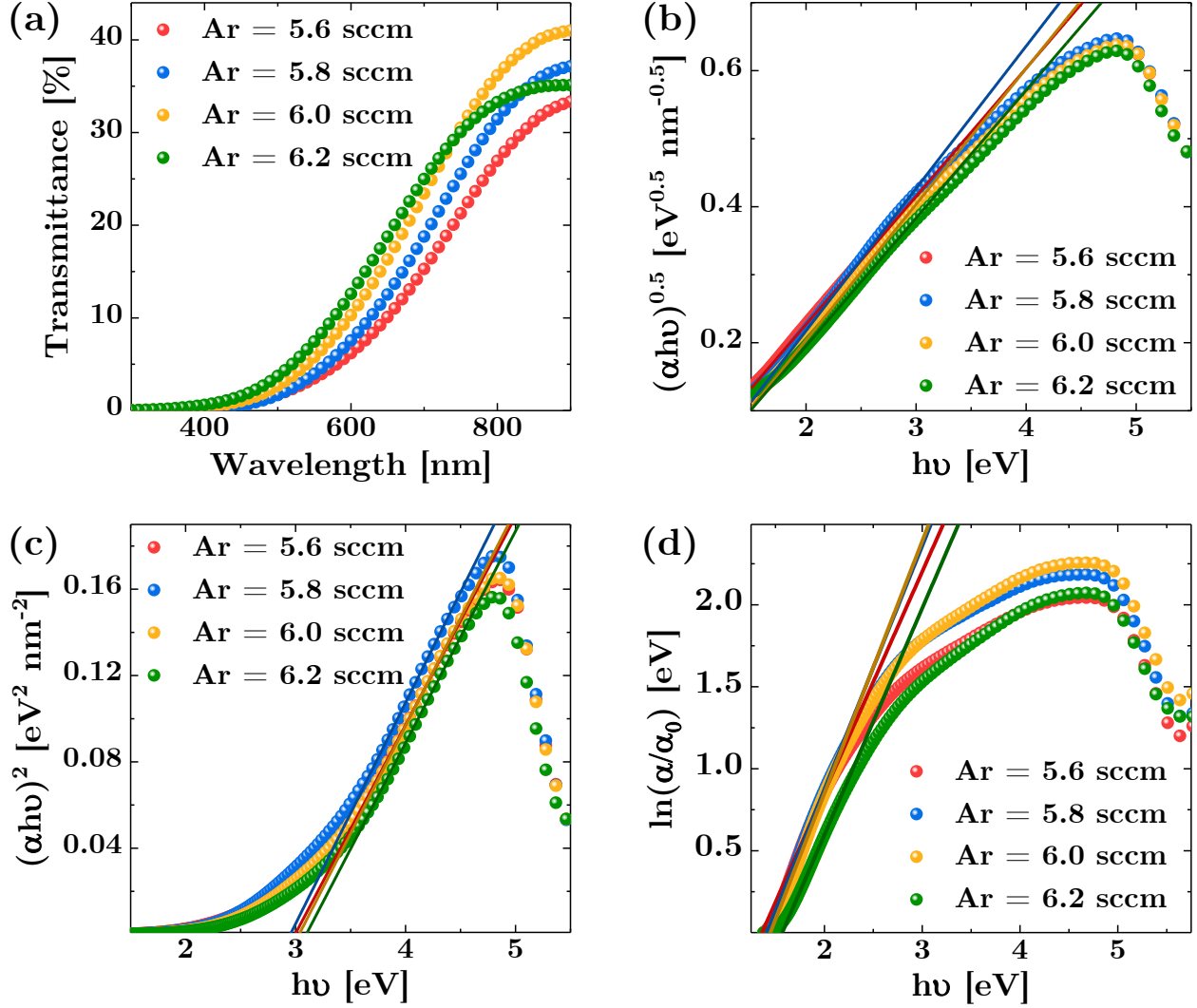
Figure S1: (a) Transmittance spectra of the SnO films with variations in argon (Ar) flow rate. Fitting procedures for (b) indirect and (c) direct bandgap extractions according to the Tauc method, as stated in Eq. S1, for γ equal to 2 and 1/2, respectively. (d) Natural logarithmic plotting for extracting the Urbach energy according to the Urbach rule, as given in Eq. S2.

as the exponential absorption edge, known as the Urbach regime.

To more precisely identify the Urbach regime, we transform the exponential function into a linear one by applying the natural logarithm to the absorbance (α) and photon energy (E)
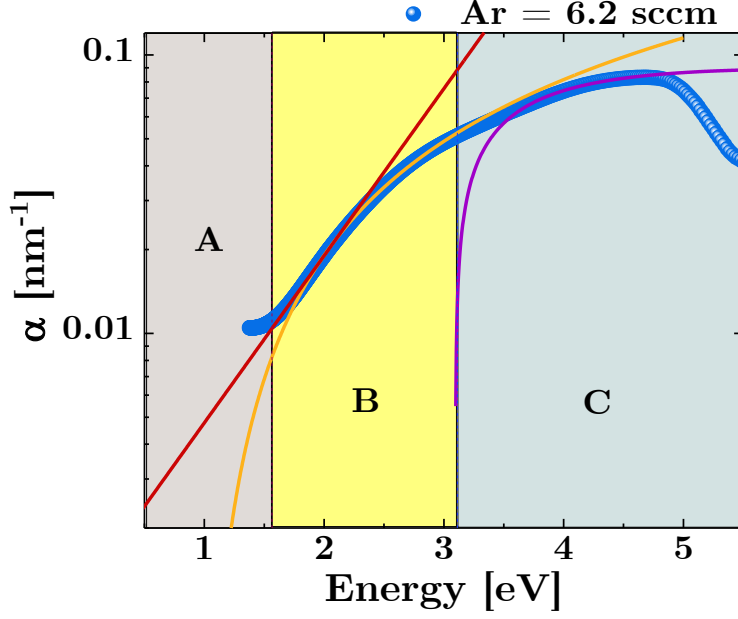
Figure S2: Semilogarithmic representation of absorption coefficient against photon energy. This plot is designed to illustrate the fitting regime, clearly delineating the three distinct regions in Tauc's framework for amorphous semiconductors. It highlights the low-energy region 'A', the high-energy region 'C', and the exponential absorption edge in the intermediate region 'B' (Urbach regime).

data, as per the following relation:

$$\alpha(E) = \alpha_0 \exp\left(\frac{E - E_{\text{gap}}}{E_{\mathbf{U}}}\right) \rightarrow \ln\frac{\alpha}{\alpha_0} = \frac{1}{E_{\mathbf{U}}}E - \frac{E_{\text{gap}}}{E_{\mathbf{U}}}$$

$$E = E_{\mathbf{U}}\ln\frac{\alpha}{\alpha_0} + \frac{E_{\text{gap}}}{E_{\mathbf{U}}}$$

(S3)

Subsequently, we identify the regime within region B that exhibits a linear trend. We then conduct linear regression $(y = mx + c)$ over a carefully chosen range within this linear regime. This regression provides the slope (m), which is crucial for calculating Urbach energy $(E_U = 1/m)$.

S1.2   Error Analysis

To evaluate precision, we conduct an error analysis, which includes calculating the standard deviation of the residuals. This step assesses the fit's accuracy and gauges the deviation of

observed data from our regression model. Error propagation due to multiplication or division is estimated through the following relation:

$$\frac{\sigma_x}{x} = \sqrt{\left(\frac{\sigma_a}{a}\right)^2 + \left(\frac{\sigma_b}{b}\right)^2 + \left(\frac{\sigma_c}{c}\right)^2} \tag{S4}$$

This formula allows us to calculate the standard deviation for parameters derived from the slope and/or y-intercept in the linear fitting. For instance, considering $E_{\text{gap}}^{\text{direct}} = c_1/m_1$ from the Tauc fitting method, the error can be estimated as:

$$\frac{\Delta E_{\text{gap}}^{\text{direct}}}{E_{\text{gap}}^{\text{direct}}} = \sqrt{\left(\frac{\Delta m_1}{m_1}\right)^2 + \left(\frac{\Delta c_1}{c_1}\right)^2} \tag{S5}$$

Similarly, for the Urbach energy, since it is calculated from $E_U = 1/m_2$ and providing a quantifiable measure of uncertainty of the slope from the linear fitting, we can then compute the standard error of the Urbach energy: $\Delta E_U = \frac{\Delta m_2}{m_2} E_U$

S1.3 Tauc-Urbach Extractor User Interface

We utilized a home-built Python code for the fitting process to extract Urbach energy. The `NumPy polyfit` function is employed for linear fitting of the data, which includes obtaining the standard deviation of the fit. This regression yields the slope (m_2), crucial for calculating the Urbach energy $(E_U = 1/m_2)$.

A user-friendly interface has been developed using Python and QT-Designer. It is accessible *via* the GitHub link provided below:

https://github.com/moch-januar/Tauc-Urbach_Extractor

This interface encapsulates the algorithm for Urbach energy extraction as well as the Tauc methods for bandgap determination. It enables users not only to easily reproduce our results but also to broadly apply the concepts, especially in extracting Urbach energy and the band gap of materials through transmittance measurements using UV-visible spectroscopy.

S2 Refractive Index Calculations

S2.1 Obtaining Complex Refractive Index from UV-visible Spectrum

The analytical method proposed by Nichelatti[7] offers a formula for determining the complex refractive index, $\tilde{n} = n + i\kappa$, of a slab dielectric layer based on its transmittance and reflectance data.

$$
\begin{aligned}
n &= \frac{1 + R_F}{1 - R_F} + \sqrt{\frac{4R_F}{(1 - R_F)^2} - \kappa^2} \; , \\
\kappa &= \frac{\lambda}{4\pi d} \ln\left(\frac{R_F T}{R - R_F}\right) \; .
\end{aligned}
\tag{S6}
$$

Here, the reflectance coefficient, R_F, is deduced from the measured reflectance (R) and transmittance (T) in a UV-visible setup, as expressed by the following equation:

$$
R_F = \frac{2 + T^2 - (1 - R)^2 - \sqrt{[2 + T^2 - (1 - R)^2]^2 - 4R(2 - R)}}{2(2 - R)} \; .
\tag{S7}
$$

S2.2 Interpolation of the Refractive Index Database for Metallic-Sn

To establish a reference point for the refractive index value of the β-Sn metallic phase, we performed interpolation using literature databases. Figure S3 displays refractive index data from the works of Palik[8] and Golopashkin-Motulevich.[9] Each database provides values for both shorter and longer wavelengths relative to the visible light spectrum. However, recognizing the lack of comprehensive data in the visible light regime in these sources, we conducted cubic b-spline interpolation of both databases. This interpolation process led us to estimate the refractive index of β-Sn to be approximately 1.48 at 550 nm, the wavelength at which we evaluated the refractive index for our SnO samples.
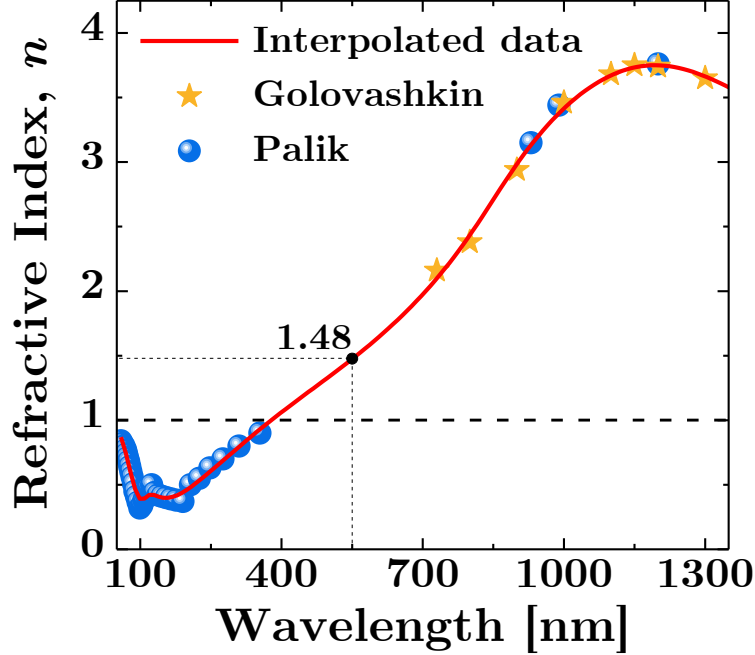
Figure S3: Refractive index databases for metallic Sn with cubic b-spline interpolation for the visible light regime.

S3 X-ray Photoelectron Spectroscopy (XPS) Analysis

In this section, we present the XPS survey scan and binding energy calibration using gold (Au) $4f$ and carbon (C) $1s$ spectra. We also detail the spectral deconvolution of the sample prior to argon (Ar) sputtering, as well as the comparison of elemental atomic percentages in the samples before and after Ar sputtering.

S3.1 Elemental Atomic Concentrations in the SnO Films

The survey scan, as given in Figure S4, reveals the presence of four elemental atoms in the samples: Sn (Tin), O (Oxygen), Au (Gold), and C (Carbon). We analyzed these elements under varying conditions, including depth profiling before and after 1 kV Ar sputtering for 180 s. The atomic concentrations are presented in the following tables:
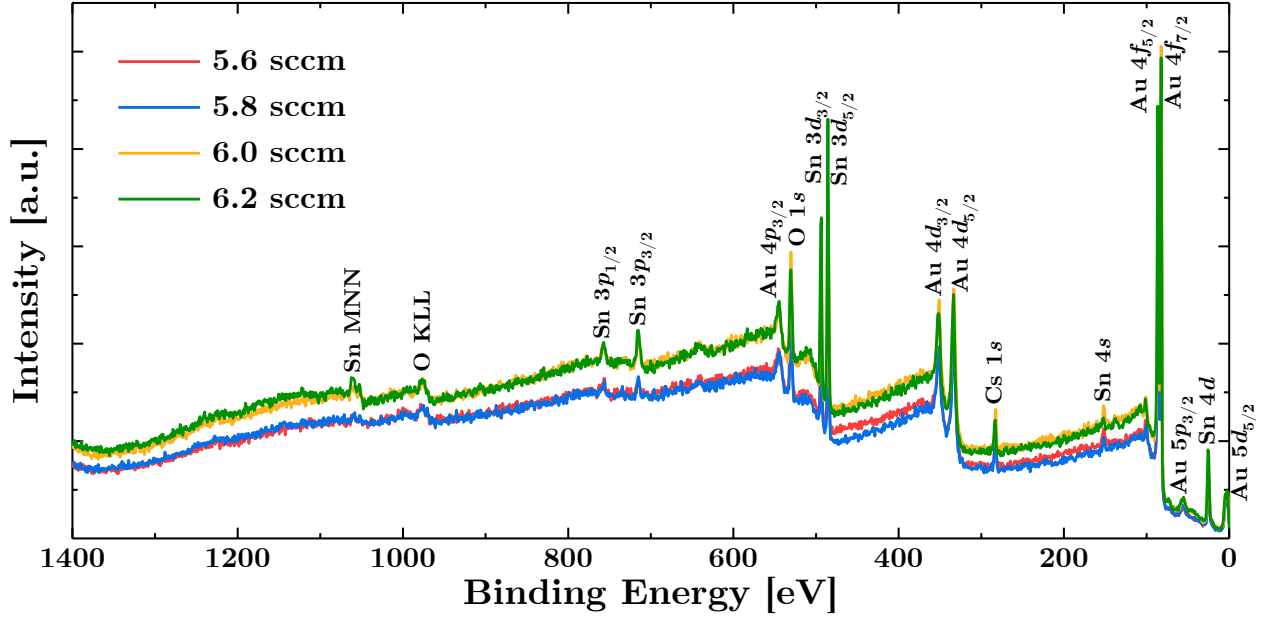
Figure S4: X-ray photoelectron spectroscopy (XPS) survey scan showing the composition of SnO films with variations in argon (Ar) flow rate.

Table S1: Elemental Atomic Concentration (Without Ar Sputtering)

Ar flow rate [sccm]	Sn $3d$ [%]	O $1s$ [%]	C $1s$ [%]	Au $4f$ [%]
5.6	7.40	30.21	45.01	17.38
5.8	8.11	30.29	43.73	17.87
6.0	9.30	30.57	41.88	18.25
6.2	11.78	29.14	41.04	18.04

Table S2: Relative Concentration between Sn and O Atoms (Without Ar Sputtering)

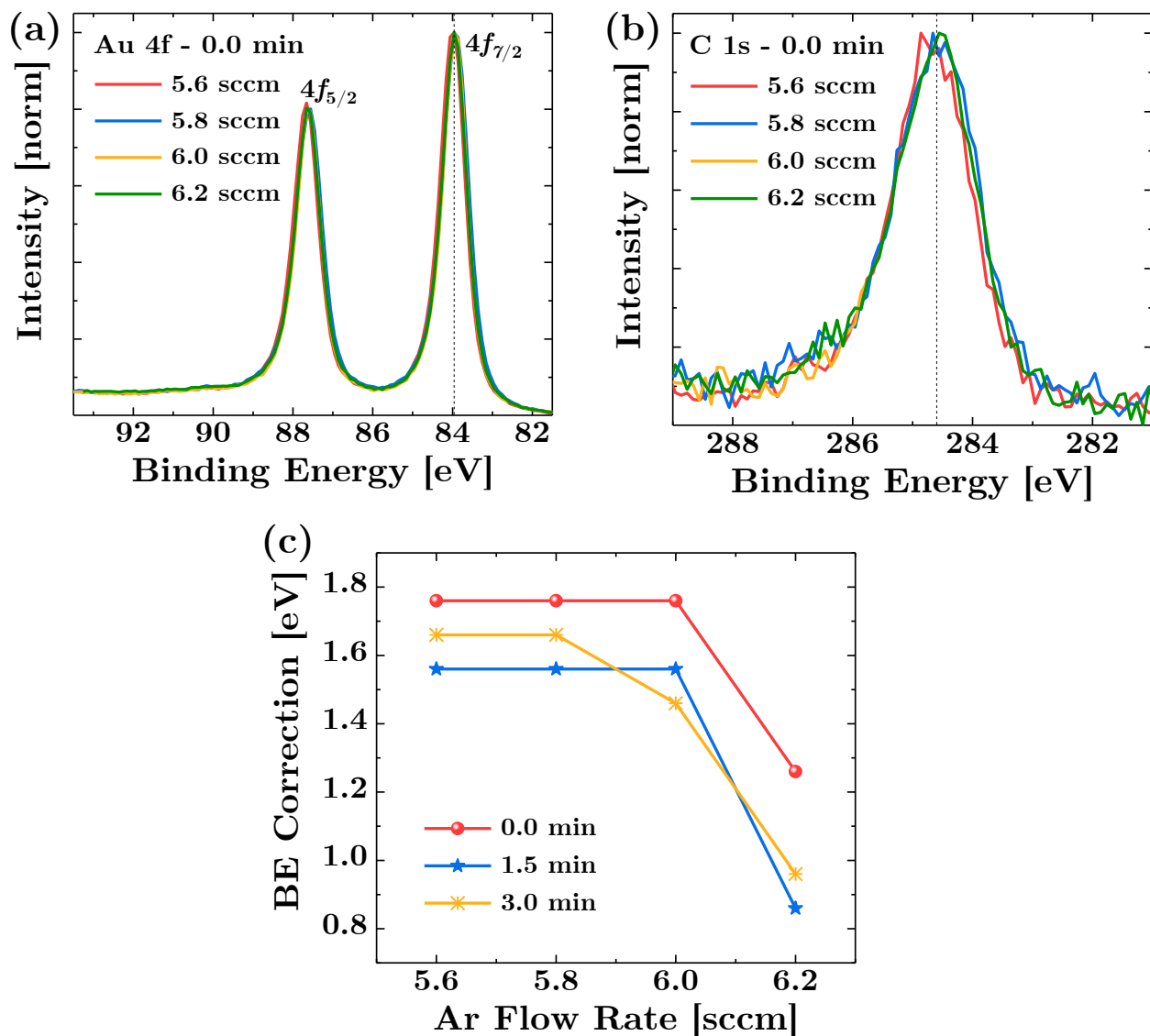| Ar flow rate [sccm]	Sn $3d$ [%]	O $1s$ [%]	O/Sn
5.6	7.40	30.21	4.08
5.8	8.11	30.29	3.74
6.0	9.30	30.57	3.29
6.2	11.78	29.14	2.47

Figure S5: (a) Au $4f$ spectral matching for XPS binding energy calibrations of SnO films with variations in Ar flow rate. (b) Confirmation of the calibrated binding energy using the C $1s$ spectra. (c) Binding energy correction for each sample, accounting for varying depth profiles based on different Ar sputtering times using a 1 kV sputter energy.

Table S3: Elemental Atomic Concentration (1 kV Ar Sputtering for 180 s)

Ar flow rate [sccm]	Sn $3d$ [%]	O $1s$ [%]	C $1s$ [%]	Au $4f$ [%]
5.6	24.93	42.40	0	32.67
5.8	26.68	43.66	0	29.66
6.0	25.74	41.89	0	32.37
6.2	26.77	42.16	0	31.07

Table S4: Relative Concentration between Sn and O Atoms (1 kV Ar Sputtering for 180 s)

Ar flow rate [sccm]	Sn $3d$ [%]	O $1s$ [%]	O/Sn
5.6	37.03	62.97	1.70
5.8	37.93	62.07	1.64
6.0	38.06	61.94	1.63
6.2	38.84	61.16	1.58

S3.2 Interpreting Higher Binding Energy Peaks in O $1s$ XPS Spectra

As illustrated in Figure S6(b) and Figure 4(b) (main text), the O $1s$ XPS analysis of the SnO film fabricated at room temperature shows peaks at 532.55 eV, 531.7 eV, 530.4 eV, and 529.9 eV. The latter two peaks can confidently be attributed to lattice oxygen bound to tetravalent tin $(O-Sn^{4+})$ and divalent tin $(O-Sn^{2+})$, respectively, as supported by various literature sources.[10,11] However, the assignment of the first two peaks might vary depending on the film preparation conditions. For our film, we have assigned the 532.55 eV peak to adsorbed oxygen or $-OH$ groups from the environment. While some studies assign the peak at 531.7 eV to adsorbed $-OH$ groups, this does not appear to be the case for our film. Unlike the 532.55 eV peak, which disappears, the 531.7 eV peak remains even at deeper depth profiles after sputtering with Ar at 1 kV for 180 s. Similar observations in the literature suggest that this peak could be attributed to the formation of O_2 molecules within the lattice oxygen.[12,13]

Furthermore, the assignment of the 531.7 eV peak to unbound oxygen in the films aligns with our observation of O/Sn atomic concentration ratios exceeding 1.5 in all the IBAD-fabricated SnO films, indicative of an O-rich state. Given the absence of thermal annealing during fabrication, there is no additional thermal budget to force excess oxygen to bind to Sn.
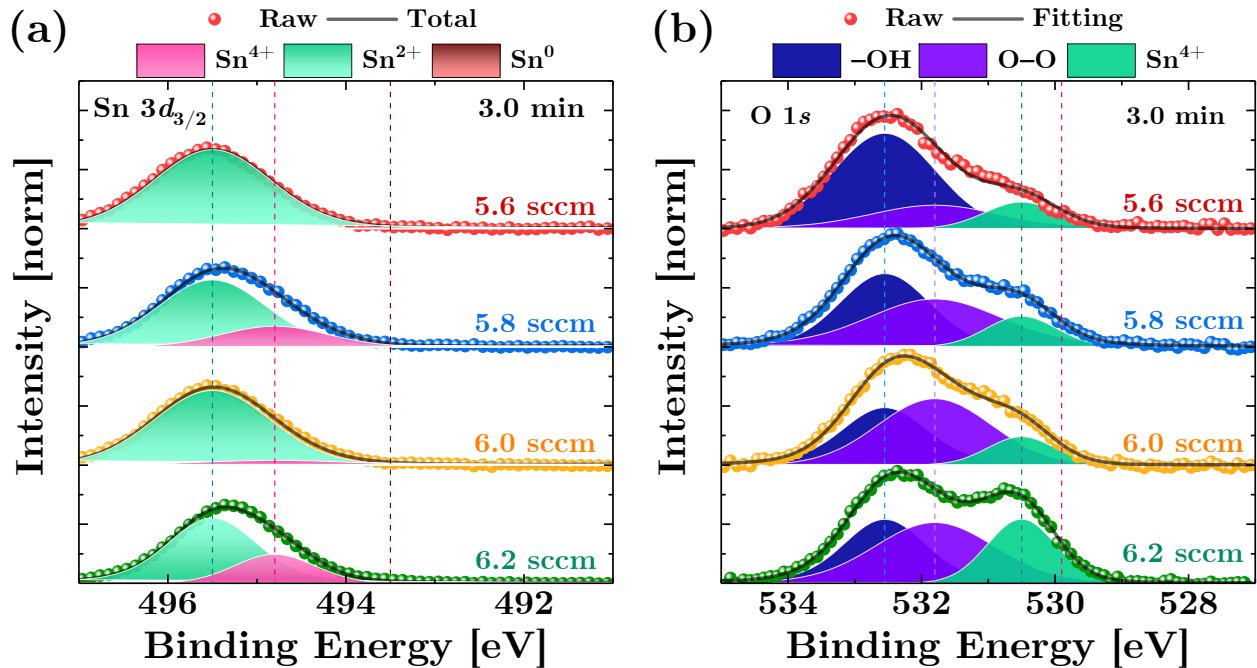
Figure S6: Deconvoluted high-resolution spectra of (a) Sn $3d$ and (b) O $1s$ orbitals at the film surface, acquired without performing Ar sputtering prior to the XPS signal acquisitions.

S4 Discrepancy in Sn $3d$ and O $1s$ XPS Spectra of Nanocrystalline SnO Film: A Combined XPS and Raman Spectroscopy Analysis

Due to the apparent discrepancy in Sn valence states between parts (a) and (b) in Figure 4, our analysis indicates a complex interaction between Sn oxidation states and the oxygen environment in the SnO films. This complexity is a result of the room-temperature fabrication process, which produces SnO with a strongly disordered lattice structure, manifesting as nanocrystalline, as indicated by Urbach rule analysis, XRD, AFM, and FE-SEM data. Consequently, the analysis of the XPS data will be less straightforward than that of a conventional polycrystalline SnO film.

To provide more clarity, Figure S7 presents the XPS and Raman spectra for the samples processed at 6.2 sccm. This figure also includes the relative areas of the deconvoluted peaks for the O $1s$ and the Raman spectra. These figures illustrate the balanced presence
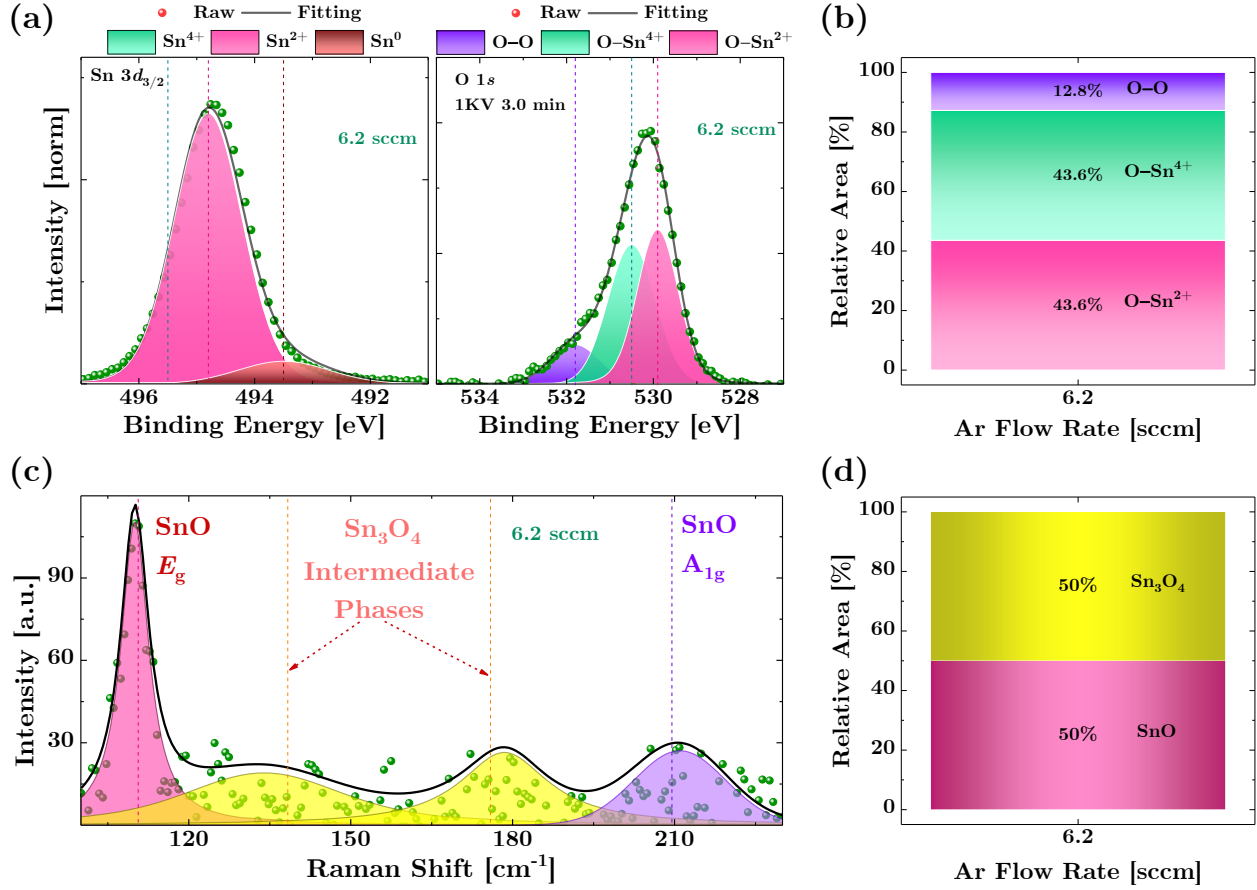
Figure S7: Combined XPS and Raman Spectroscopy Analysis of SnO Sample Fabricated with a 6.2 sccm Ar Flow Rate: (a) XPS spectra showcasing the Sn $3d_{3/2}$ and O $1s$ states. (b) Relative area analysis of the O $1s$ deconvoluted spectra, illustrating the distribution of different oxygen states. (c) Raman spectra highlighting the vibrational modes specific to the SnO sample. (d) Relative area analysis of the deconvoluted spectra for Sn_3O_4-likeè and SnO phases, demonstrating the proportions of these phases in the sample.

of $O-Sn^{2+}$ and $O-Sn^{4+}$ states, indicative of a 1:1 ratio (see Figure S7(a) and (b)), which is mirrored in the Raman data. As shown in Figure S7(c) and (d), the total areas of the Raman peaks near 138 cm^{-1} and 176 cm^{-1} (linked to the formation of Sn_3O_4-like interme- diate phases[14,15]) and those near 110 cm^{-1} and 210 cm^{-1} (associated with SnO phases[16–18]) also display a similar 1:1 ratio. This suggests a coexistence of SnO and Sn_3O_4-like phases. Significantly, this finding corroborates our interpretation that the formation of sub-oxides, along with the SnO phase, accounts for the discrepancies observed in the Sn $3d$ and O $1s$ XPS spectra. Thus, these correlations affirm that the variations in the Sn $3d$ and O $1s$ XPS

spectra are indicative of the formation of sub-oxides, in conjunction with the SnO phase. This is further underlined by the Raman data, which points to the Sn_3O_4-like intermediate phase.

References

1. Makula, P.; Pacia, M.; Macyk, W. How To Correctly Determine the Band Gap Energy of Modified Semiconductor Photocatalysts Based on UV-Vis Spectra. *J. Phys. Chem. Lett.* **2018**, *9*, 6814–6817.

2. Yu, E. K.-H.; Jun, S.; Kim, D. H.; Kanicki, J. Density of States of Amorphous In−Ga−Zn−O from Electrical and Optical Characterization. *J. Appl. Phys.* **2014**, *116*, 154505–154510.

3. Fung, T.-C.; Chuang, C.-S.; Nomura, K.; Shieh, H.-P. D.; Hosono, H.; Kanicki, J. Photofield-Effect in Amorphous In-Ga-Zn-O (a-IGZO) Thin-Film Transistors. *J. Inf. Disp.* **2008**, *9*, 21–29.

4. Cody, G. D. Urbach Edge of Crystalline and Amorphous Silicon: A Personal Review. *J. Non-Cryst. Solids* **1992**, *141*, 3–15.

5. Rai, R. C. Analysis of the Urbach Tails in Absorption Spectra of Undoped ZnO Thin Films. *J. Appl. Phys.* **2013**, *113*, 153508–153512.

6. Tauc, J. Absorption Edge and Internal Electric Fields in Amorphous Semiconductors. *Mater. Res. Bull.* **1970**, *5*, 721–729.

7. Nichelatti, E. Complex Refractive Index of a Slab From Reflectance and Transmittance: Analytical Solution. *J. Opt. A: Pure Appl. Opt.* **2002**, *4*, 400–403.

8. Palik, E. D. *Handbook of Optical Constants of Solids*; Academic Press, Maryland, 1985.

9. Golovashkin, A. I.; Motulevich, G. P. Optical and Electrical Properties of Tin. *Sov. Phys. JETP* **1964**, *19*, 310–317.

10. Choi, W.; Jung, H.; Koh, S. Chemical Shifts and Optical Properties of Tin Oxide Films Grown by a Reactive Ion Assisted Deposition. *J. Vac. Sci. Technol., A* **1996**, *14*, 359–366.

11. Jiménez, V.; Mejías, J.; Espinós, J.; González-Elipe, A. Interface Effects for Metal Oxide Thin Films Deposited on Another Metal Oxide II. SnO_2 Deposited on SiO_2. *Surf. Sci.* **1996**, *366*, 545–555.

12. Wang, J.; Hu, C.; Xia, Y.; Zhang, B. Mesoporous ZnO Nanosheets with Rich Surface Oxygen Vacancies for UV-Activated Methane Gas Sensing at Room Temperature. *Sens. Actuators B: Chem.* **2021**, *333*, 129547–129555.

13. Kotsis, K.; Staemmler, V. Ab Initio Calculations of the O1s XPS Spectra of ZnO and Zn Oxo Compounds. *Phys. Chem. Chem. Phys.* **2006**, *8*, 1490–1498.

14. Shanmugasundaram, A.; Basak, P.; Satyanarayana, L.; Manorama, S. V. Hierarchical SnO/SnO_2 Nanocomposites: Formation of in situ *p-n* Junctions and Enhanced H_2 Sensing. *Sensors and Actuators B: Chemical* **2013**, *185*, 265–273.

15. Januar, M.; Prakoso, S. P.; Zhong, C.-W.; Lin, H.-C.; Li, C.; Hsieh, J.-H.; Liu, K.-K.; Liu, K.-C. Room-Temperature Fabrication of p-Type SnO Semiconductors Using Ion-Beam-Assisted Deposition. *ACS Applied Materials & Interfaces* **2022**, *14*, 46726–46737.

16. Liu, L.; Wu, X.; Li, T.; Shen, J. Correlation of the 755-778 cm^{-1} Raman Mode with Oxygen Vacancies in Tin Oxide Nanostructures. *Applied Surface Science* **2015**, *347*, 265–268.

17. Luo, H.; Liang, L. Y.; Cao, H. T.; Liu, Z. M.; Zhuge, F. Structural, Chemical, Optical,

and Electrical Evolution of SnO_x Films Deposited by Reactive RF Magnetron Sputtering. *ACS Applied Materials & Interfaces* **2012**, *4*, 5673–5677.

18. Duan, Y. Electronic properties and stabilities of bulk and low-index surfaces of SnO in comparison with SnO_2: A first-principles density functional approach with an empirical correction of van der Waals interactions. *Phys. Rev. B* **2008**, *77*, 045332.